

Article

Microstructure and Mechanical Properties of Al-4Mg-0.3Cu Alloy after HPT and Postdeformation Annealing

Xiaohui Yang ^{1,2,3,*}, Chao Gao ^{1,2}, Tingting Ku ⁴, Wenlu Yang ^{1,2}, Yanping Guo ^{1,2,3}, Linzeng Wang ², Huiqin Chen ^{1,2}, Xiaofeng Li ⁵, Rujie Hu ² and Jianyu Cui ²

¹ Shanxi Heavy Casting and Forging Engineering Technology Research Centre, Taiyuan University of Science and Technology, Taiyuan 030024, China; 2006020@tyust.edu.cn (Y.G.)

² School of Materials Science and Engineering, Taiyuan University of Science and Technology, Taiyuan 030024, China

³ Instrumental Analysis Center, Taiyuan University of Science and Technology, Taiyuan 030024, China

⁴ College of Environmental and Resource Science, Shanxi University, Taiyuan 030006, China

⁵ School of Materials Science and Engineering, North University of China, Taiyuan 030051, China

* Correspondence: xhyang@tyust.edu.cn

Highlights:

What are the main findings?

What is the implication of the main finding?

- The effects of different strain levels and subsequent annealing treatment on the microstructural evolution of Al-4Mg-0.3Cu alloy were investigated.
- The mechanism of Cu segregation at grain boundaries was discussed in detail.
- The thermal stability of different deformed microstructures of Al-4Mg-0.3Cu alloy was evaluated.
- Al-4Mg-0.3Cu alloy subjected to HPT deformation and subsequent heat treatment exhibits high fracture strength and fracture elongation.



Citation: Yang, X.; Gao, C.; Ku, T.; Yang, W.; Guo, Y.; Wang, L.; Chen, H.; Li, X.; Hu, R.; Cui, J. Microstructure and Mechanical Properties of Al-4Mg-0.3Cu Alloy after HPT and Postdeformation Annealing. *Metals* **2023**, *13*, 810. <https://doi.org/10.3390/met13040810>

Academic Editor: Marcello Cabibbo

Received: 2 March 2023

Revised: 4 April 2023

Accepted: 18 April 2023

Published: 20 April 2023



Copyright: © 2023 by the authors. Licensee MDPI, Basel, Switzerland. This article is an open access article distributed under the terms and conditions of the Creative Commons Attribution (CC BY) license (<https://creativecommons.org/licenses/by/4.0/>).

Abstract: The effects of different strain levels applied through high-pressure torsion (HPT) deformation following annealing on the microstructural evolution, thermal stability, and mechanical properties of Al-4Mg-0.3Cu alloy were investigated. The results reveal that Cu-segregated grain boundaries (GBs) were generated in the ultrafine-grained Al-4Mg-0.3Cu alloy with high angle grain boundaries. By contrast, the phenomenon of Cu segregation was not found in micron-scale and submicron-scale grains with low-angle grain boundaries. The mechanism of Cu segregation in ultrafine-grained Al-4Mg-0.3Cu alloy was discussed. After heat treatment, Cu segregation induced the precipitation of the dense Al₂CuMg phase at GBs, which strongly inhibit grain growth and improve thermal stability. Stress–strain curves of as-cast, 5-turn, and 10-turn HPT samples showed that fracture strength significantly increased, attributed to grain size refinement, dislocation density increase, and Cu segregation at GBs. After heat treatment, 5-turn and 10-turn HPT samples demonstrate an enhanced elongation to fracture with a slight reduction of fracture strength.

Keywords: Al-4Mg-0.3Cu alloy; high-pressure torsion; microstructural evolution; thermal stability; mechanical properties

1. Introduction

Al-Mg (5xxx series) alloys are now widely used in marine applications, automotive manufacturing, and electronic areas due to their high specific strength, superior corrosion resistance, excellent processing properties, and so on [1]. The pursuit of lightweight materials for energy saving and emission reduction has led to continuous research to further increase the strength of Al-Mg alloys [2,3]. Due to the absence of nanoscale precipitates

in Al-Mg alloys, the improvement of the strength of these alloys mainly takes advantage of solid solution strengthening and grain boundary (GB) strengthening [4]. However, the higher Mg concentration (>5 wt.%) in the Al-Mg alloys deteriorates the machinability and increases the machining cost [5]. Recently, the strength of Al-Mg alloys was improved via grain size refinement to ultrafine scale using severe plastic deformation methods (SPD), such as high-pressure torsion (HPT) and equal channel angular pressing (ECAP) [6]. Among these SPD methods, HPT is one of the most effective approaches for producing exceptional grain refinement because it can impart a very large plastic strain [7]. However, these ultrafine Al-Mg alloys are thermodynamically unstable and prone to undergo rapid grain growth under mechanical loading or exposure at temperatures far below the ordinary recrystallization temperature [8]. Meanwhile, the instability of grain size easily leads to strength loss due to grain coarsening, which limits their potential applications.

To stabilize ultrafine-grained Al-Mg alloys, several strategies have been proposed to inhibit grain growth by retarding the GB mobility through solute drag [9] or second-phase particle pinning [10] and/or controlling the GB structures through GB relaxation [11] and solute segregation [12]. For example, Al-based alloys processed by HPT with enhanced thermal stability induced by segregation have been found in Al-Mg [13,14], Al-Fe [15], Al-Ca [16], and Al-Zr [17] alloys. However, Al-Zn alloy processed by HPT with GB segregation exhibits a poor longtime stability [18,19]. Minor Cu addition to Al-Mg alloy usually was utilized to eliminate softening in Al-Mg alloys during paint baking [20,21]. In addition, Cu segregation can stabilize the fine spacing lamellar structures of Al-0.3%Cu alloy during deformation and annealing [22,23]. However, the effects of trace Cu addition and different grain structures on the solute segregation behavior and thermal stability of ultrafine-grained Al-Mg alloys have been rarely reported so far.

To better understand the effects of minor Cu addition, grain structures, and annealing treatment on the GBs' segregation or precipitation behavior in Al-Mg alloys, the solute content or precipitation distribution along the GBs was characterized in the samples processed by HPT with different strains. In addition, the influence of solute segregation or solute precipitation on the thermal stability and mechanical properties of Al-Mg alloys was also studied.

2. Experimental Section

High-purity Al (99.99 wt.%), pure Mg (99.99 wt.%), and Al-4Cu master alloy (99.9 wt.%) were accurately weighted according to the Al-4Mg-0.3Cu alloy stoichiometric formula. Subsequently, the mixture of weighed material was melted in a graphite crucible heated to 760 °C and added with a slag remover. After stirring evenly for 2 min, it was quickly poured into a cylindrical steel mold and cooled at room temperature. After that, the as-cast Al-4Mg-0.3Cu alloy ingot was kept at 450 °C for 6 h for homogenization treatment, and cooled to room temperature by furnace cooling. Next, the homogenized Al-4Mg-0.3Cu alloy was processed into disk-shaped specimens with a diameter of 20 mm and a thickness of 2.0 mm by wire cutting. Both sides of the disk-shaped specimens were sanded with 2000-grit sandpaper and polishing on a polisher until the thickness of the disk-shaped specimens was 1.7 mm. Finally, the polished disk-shaped sample was processed using high-pressure torsion equipment for 1, 3, 5, and 10 turns, applying a pressure of 4 GPa. The thickness of the disk sample after high-pressure torsion processing was about 1.4 mm. In addition, T.G. Langdon et al. [24,25] demonstrated that there is very little slippage between the anvil and sample and temperature rise when thin Al alloy disks are processed by HPT.

The microstructural analysis of samples was characterized using a transmission electron microscope (TEM, Titan G2 60-300) equipped with an energy dispersive spectrometer (EDS, Super-X detector). Thin foils for TEM, HAADF-STEM observation, and electron backscatter diffraction (EBSD) pattern collection were prepared by the twin-jet polishing technique in a mixture of 30% nitric acid and 70% carbinol at −30 °C. EBSD patterns were collected on a Philips XL 30S field emission scanning electron microscope (SEM) equipped with a TSL-OIM EBSD system using a step size of 30 nm and an accelerating voltage of

30 kV. In addition, the EBSD map can be processed by a cleanup procedure in the TSL-OIM EBSD system to eliminate the nonindexed EBSD data, and the detailed information of the sample for the EBSD map is illustrated in Table 1. X-ray diffraction (XRD) patterns were measured by a Philips X'pert powder diffractometer with a Johansson monochromator, which eliminated $\text{CuK}\alpha_2$ radiation. To quantify the dislocation density evolution in samples with different strain amounts, X-ray peak profile analysis was conducted using the Williamson–Hall method [26,27]. The central part of disk samples for an XRD test was polished with sandpaper and then electropolished in an acid mixture ($\text{HNO}_3:\text{CH}_3\text{OH} = 1:3$). In addition, the locations for the TEM, EBSD, and XRD foil specimen are illustrated in Figure 1a. An FEI-VM50 PC Vickers hardness testing machine was used to characterize the inhomogeneity of specimens with a load 100 g and a 15 s dwell time. Microhardness data were obtained by averaging measurements taken at discrete locations along two mutually perpendicular diameters at a step of 0.5 mm of the HPT-processed samples with different revolutions, as illustrated in Figure 1a. The tensile specimens with a dog bone shape were machined from the disk samples, as shown in Figure 1b. The strain-respectful position curves from the disk samples are shown in Figure 1c,d, and the positions labeled as A, B, C, D, E, and F are marked by black circles. The mechanical properties of tensile specimens were performed using an American Instron 3369 mechanical testing instrument at a constant strain rate of 5×10^{-4} s. To ensure the consistency and repeatability of the experiment, each type of sample was subjected to three parallel experiments.

Table 1. Information of samples for EBSD analysis.

Sample Position	Test Area (μm^2)	Value of Confidence Index (%)	Sample Conditions (Annealing Treatment)
Position E in Figure 2	12	70	200 °C for 10 min
Position F in Figure 2	3	60	200 °C for 10 min
Position E in Figure 2	96	85	200 °C for 1 h

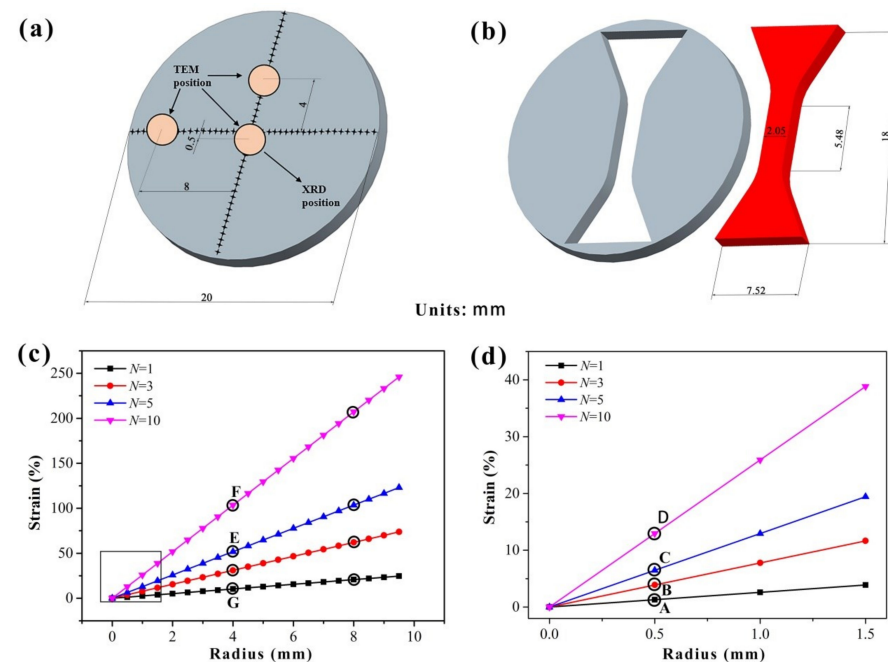


Figure 1. (a) Schematic diagram of measurement positions in the HPT disk specimen for Vickers microhardness measurement and microstructural analysis; (b) position extracted for tensile specimen with dimensions; (c) curves of strain-respectful position for TEM observation; (d) magnified strain-position pattern for the region marked by a black box in Figure 1c.

3. Results

Figure 2 displays the hardness evolution as a function of the von Mises equivalent strain for the as-cast and the disk samples processed by HPT for 1, 3, 5, and 10 revolutions. The von Mises equivalent strain for as-HPT processed samples can be calculated based on the formula $\varepsilon = 2\pi Nr / \sqrt{3}h$ (N is the number of turns, r is the radius of the disk, and h is the disk thickness) [28], so the strain from the central region of disk samples is 0. In fact, the hardness values from the central region of the disks gradually increases with increasing torsion turns. The phenomenon has been explained based on the strain gradient plasticity theory [29]. It can be seen from Figure 2 that when the equivalent strain is below 80, the hardness value increases with the increasing strain. Additionally, the hardness value for the equivalent strain beyond 80 has reached a stable state with 20 Hv minor fluctuations. Moreover, under the same strain with different twisting turns, the corresponding hardness values from samples are slightly different as marked by a black arrow in Figure 2.

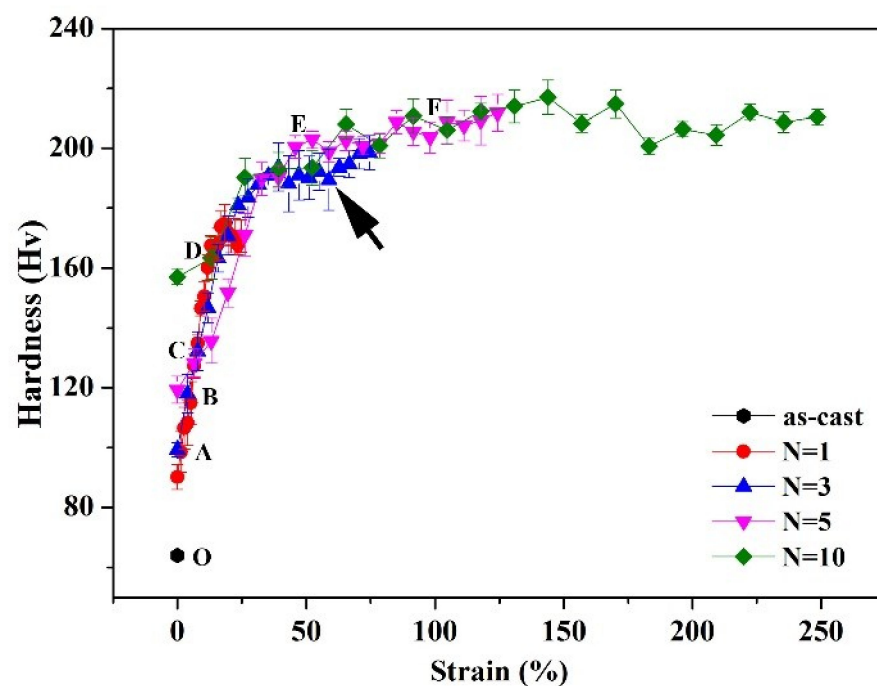


Figure 2. Average Vickers hardness plotted as a function of strains ~ 1 for A, ~ 3.5 for B, ~ 6.5 for C, ~ 13 for D, ~ 50 for E, ~ 100 for F of the as-cast and HPT processed Al-4Mg-0.3Cu alloy after 1, 3, 5, and 10 turns.

XRD patterns from the as-cast sample and the central region of as-HPT processed disk specimens with 1, 3, 5, and 10 revolutions are presented in Figure 3a. For all the sample conditions, no additional diffraction peaks are detected other than those representing the Al matrix. In addition, each diffraction peak is significantly broadened due to grain size refinement and dislocation density evolution subjected to different torsion turns. Figure 3b displays that the (220) diffraction peak of the as-cast and HPT samples for 1, 3, 5, and 10 turns gradually broadened with increasing HPT turns. The broadening of the XRD profile of HPT-processed samples is aroused by lattice defects, which are predominantly dislocations and additional grain boundaries. Figure 3c demonstrates a plot of $FWHM \times \cos(\theta)$ against $2\sin(\theta)$ for the (111), (200), (220), and (311) diffraction pattern, where the slope corresponds to the effective strain. Based on the liner fitting, it can be concluded that the effective strain of the central region from high-pressure torsional Al-4Mg-0.3Cu samples for 0, 1, 3, 5, and 10 revolutions are 0.0007, 0.0013, 0.0024, 0.0025, and 0.0022. According to the relationship between the effective strain and dislocation density (ρ) using the Williamson–Hall method [30], it can be concluded that the dislocation density is

$0.86 \times 10^{14} \text{ m}^{-2}$, $2.96 \times 10^{14} \text{ m}^{-2}$, $10.11 \times 10^{14} \text{ m}^{-2}$, $10.97 \times 10^{14} \text{ m}^{-2}$, and $8.49 \times 10^{14} \text{ m}^{-2}$ for as-cast and as-HPT processed samples with 1, 3, 5, and 10 turns, as plotted in Figure 3d. The values of dislocation density in this experiment were in good agreement with a recent report for an Al-Cu-Mg alloy processed by HPT through 5 turns measured using X-ray diffraction line broadening [31].

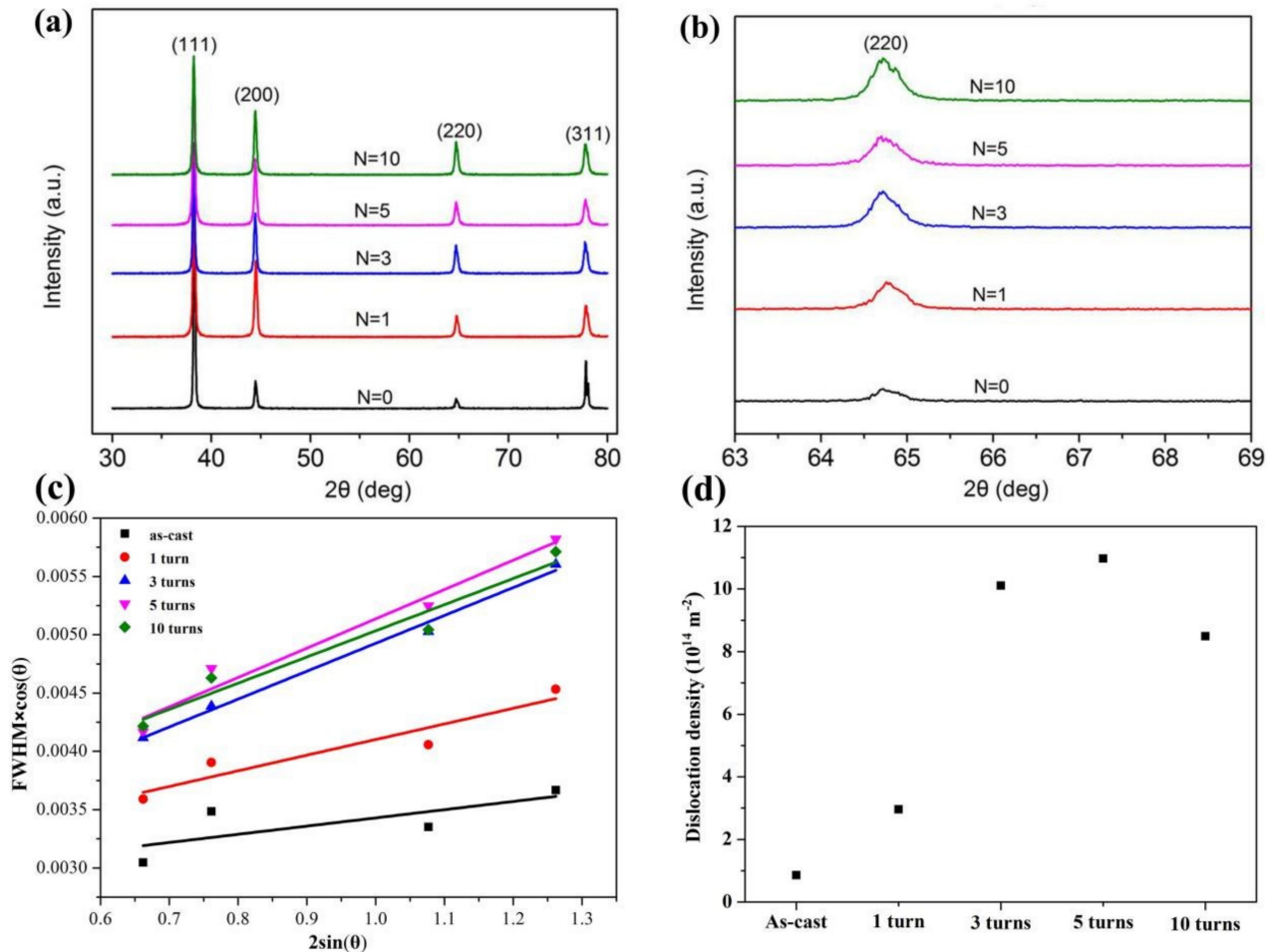


Figure 3. (a) XRD patterns the from central region of HPT Al-4Mg alloy sample for 0, 1, 3, 5, and 10 turns; (b) magnified (220) diffraction peak from samples subjected to different turns; (c) FWHM $\times \cos(\theta)$ against $2\sin(\theta)$ plots for the (111), (200), (220), and (311) diffraction patterns; (d) dislocation density evolution graph in Al-4Mg-0.3Cu alloy subjected to HPT processing.

To further investigate the microstructural features of Al-4Mg-0.3Cu alloy with different hardness values, the TEM micrographs from samples corresponding to locations A, B, C, D, E, and F illustrated in Figure 2 are shown in Figure 4a–f. It can be seen from Figure 4a that the microstructure of the sample corresponding to strain ~ 1 contains many microscopic bands with different orientations, and there are a large number of dislocations within the microscopic bands. Corresponding to the hardness value of position B in Figure 2, the microstructure shows that dislocations entangle with each other and even evolve into dislocation cells, which subdivide the deformation bands, as demonstrated in Figure 4b. As the deformation amount increases, the dislocation cells gradually transform to superfine grains, and a lot of dislocations are pinned inside these superfine grains, as shown in Figure 4c. Additionally, measurements gave an average grain size of $\sim 1.4 \mu\text{m}$ based on a statistical evaluation from several TEM images. With the further increase in torsional straining, the grain size is further refined to submicron scale, as shown in Figure 4d. Obviously, corrugated grain boundaries and dislocation tangles could be seen in ultrafine

grains and/or subgrains, as demonstrated in Figure 4d, indicating a high local strain and a high density of dislocations existing inside the grains, which confirms the nonequilibrium character. Figure 4e displays that a submicron-sized near-randomly oriented polycrystalline structure has been developed, and the visible fringes induced by interstress was frequently observed. With further increase in the amount of strain, equiaxed ultrafine grains with sharp and clean grain boundary structures and random orientations are formed, as shown in Figure 4f. In addition, through statistical measurement of about 50 grains in samples corresponding to hardness values for D, E and F, the average grain sizes were ~ 300 , ~ 140 , and ~ 100 nm, respectively.

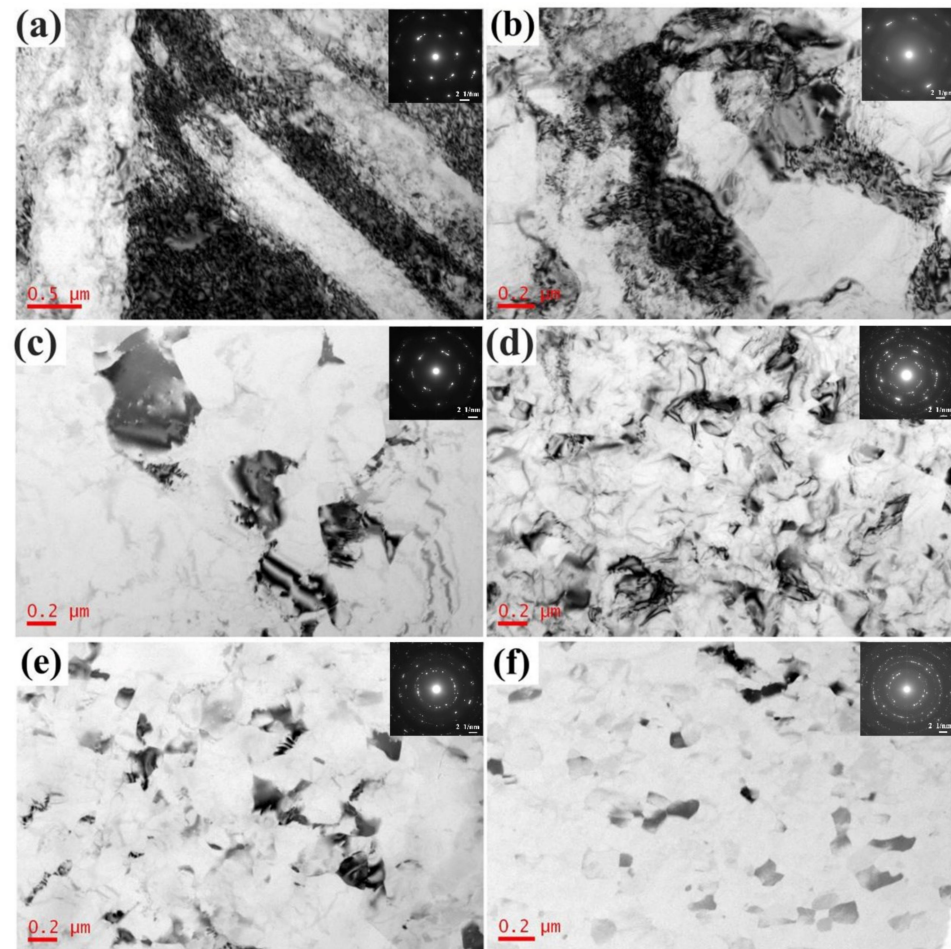


Figure 4. Microstructure micrographs of HPT processed Al-4Mg-0.3Cu alloy in Figure 4 (a–f) corresponding to locations A, B, C, D, E, and F in Figure 2 with different stains, respectively.

Due to a high dislocation density at GBs in the severely deformed samples, results were in blurred or nonexistent diffraction patterns and very low indexing rates. Therefore, the samples from locations E and F corresponding to equivalent strains 50 and 100 for EBSD pattern collection were heated to 200 °C for 10 min. Figure 5a,c demonstrate the EBSD inverse pole figure (IPF) maps of HPT-processed Al-4Mg-0.3Cu samples for locations E and F equivalent strains 50 and 100, where grain colors represent the various orientations of the grains, as denoted by the unit triangle in Figure 5a. Figure 5b,d show the evolution statistics histogram of the grain boundary misorientation of HPT-processed Al-4Mg-0.3Cu alloy for different strains. Comparing Figure 5b,d, it can be seen that the high-angle grain boundary fractions increase from 80% to 95% with increasing strain.

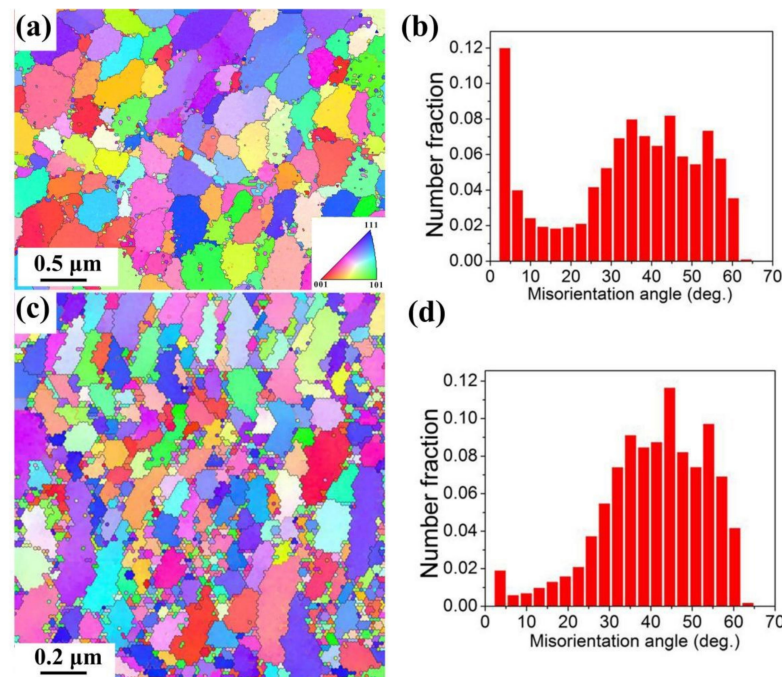


Figure 5. EBSD IPF maps of a sample from locations E and F after annealing treatment at 200 °C for 10 min; (a,c) show the EBSD IPF maps of samples from locations E and F after annealing treatment at 200 °C for 10 min; (b,d) show the corresponding histograms of the misorientation angles.

Figure 6 shows the TEM micrographs, high-angle angular dark-field scanning transmission electron microscopy (HADDF-STEM) micrographs, and EDS line scanning of samples with different strain levels. Figure 6a shows a TEM micrograph of a sample from location G in Figure 1c corresponding to a torsional strain of ~10, which demonstrates that a lot of elongated grains have been generated and a high density of dislocations in the elongated grains still exist. For the samples from locations E and F in Figure 1c with strains of 50 and 100, the microstructure mainly comprises equiaxed grains with an average grain size ~140 and ~100 nm, respectively, as shown in Figure 6d,g. To exhibit local composition changes across grain boundaries, the HADDF-STEM images from a partial area of Figure 6a,d,g provide Z contrast images, as displayed in Figure 6b,e,h. Obviously, there is no apparent difference in brightness between the intragranular and grain boundary in Figure 6b,e, and the bright segregation appears in the GBs in Figure 6h. To further confirm the composition changes of a sample subjected to different strain levels, EDS line scanning was performed along the arrows plotted in Figure 6b,e,h. EDS analysis in Figure 6c clearly demonstrates that the contents of Al, Cu, and Mg do not differ significantly within grains and grain boundaries. With the increase in deformation amount, the Cu and Mg contents are slightly higher and the Al content is lower at the grain boundary compared with those in the grain interior, as illustrated in Figure 6f. EDS analysis (Figure 6i) was carried out in ultrafine grains with equilibrium high-angle grain boundaries, and it was found that the solute Cu concentration along GBs beyond 2 at.% in Figure 6i and solute Mg content rapidly decrease. The aforementioned microstructural evolution features can be summarized as follows: (i) the solute Cu segregation at GBs only occurs when the Al-4Mg-0.3Cu alloy was refined to the ultrafine scale; (ii) compared with solute Mg, solute Cu is more prone to segregation at GBs.

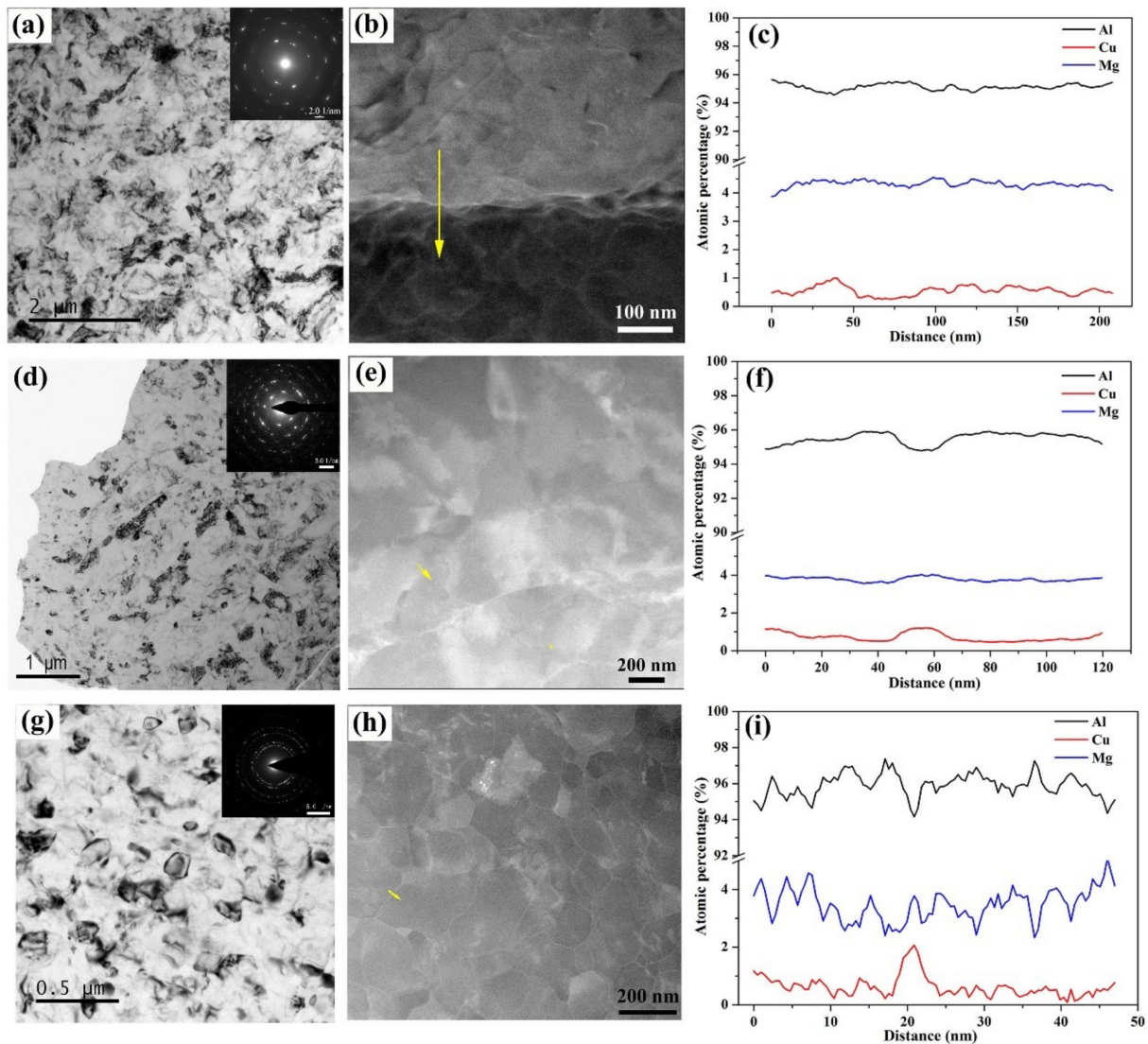


Figure 6. TEM and HADDF-STEM images of the HPT processed samples for strain 10 (a,b), 50 (d,e), and 100 (g,h); (c,f,i) demonstrate the corresponding EDS line-scanning profiles of Al, Cu, and Mg elements along the yellow arrow in Figure 6 (b,e,h), respectively.

To evaluate the thermal stability of different grain structures of Al-4Mg-0.3Cu alloy under different amounts of strain, these samples were annealed at 200 °C for 1 h, and the corresponding micrographs are shown in Figure 7. The TEM and HADDF-STEM images of the samples corresponding to strains for 10, 50, and 100 after annealing treatment are shown in Figure 7a–f. The irregular-shaped precipitates were found at GBs, and the rodlike precipitates formed inside the grains, as displayed in Figure 7b. With the strain amount increase to 50, the irregular precipitates are seen inside grains and along GBs, as displayed in Figure 7d. When the strain amount increases to 100, most of the precipitates are distributed along the grain boundaries, and a few precipitates appear inside the grains. Obviously, the size, morphology, and distribution of the precipitates are significantly affected by grain structures of the sample, which is closely related to torsional strain amount. In addition, the average grain sizes of the samples subjected to strain amounts of 10, 50, and 100 after heat treatment are 1.2 μm, 800 nm, and 300 nm by a statistical measurement of about 60 grains, respectively. Therefore, the fine and dense distributed precipitates at GBs severely reduce the growth rate of the UFG Al-4Mg-0.3Cu alloy during the heat treatment process.

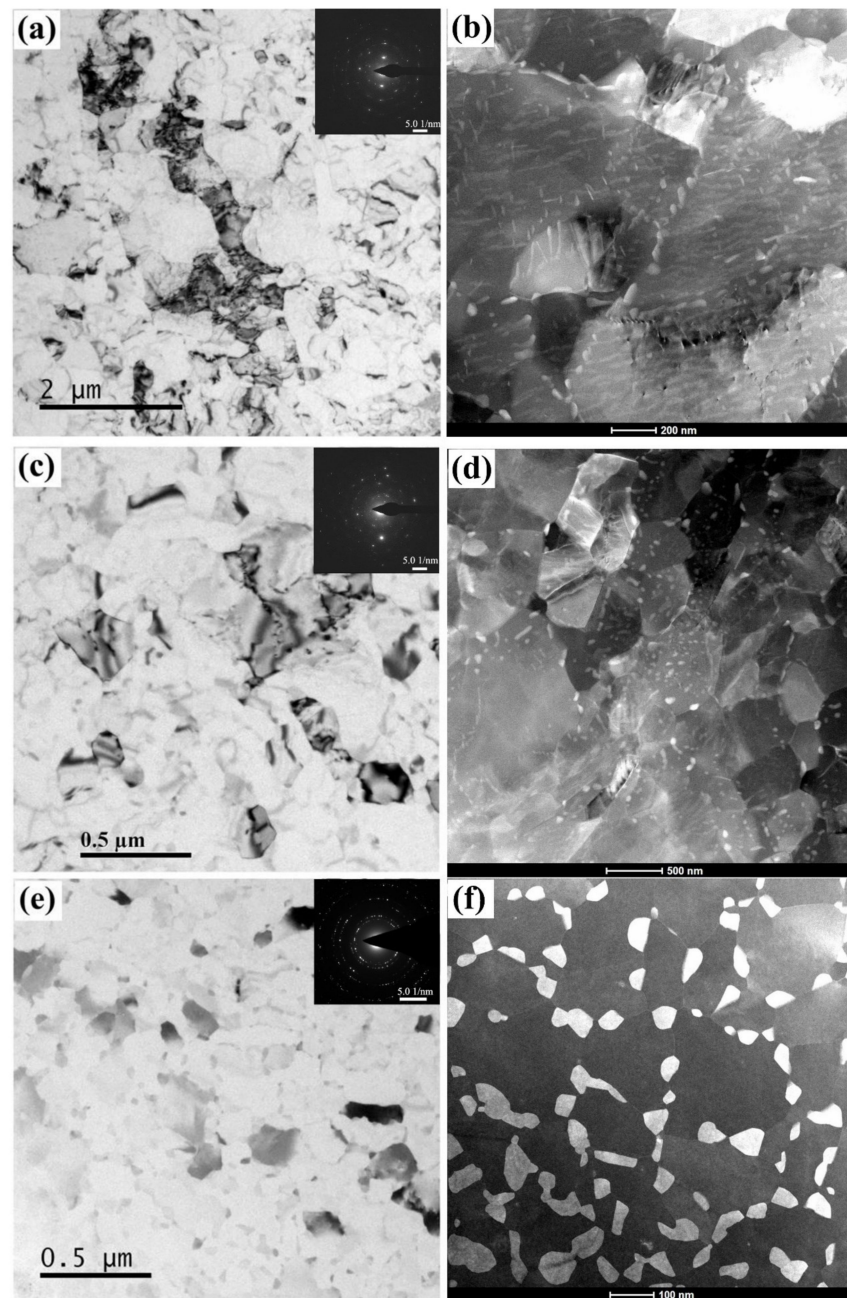


Figure 7. TEM and HADDF-STEM images of the HPT processed sample aged at 200 °C for 1 h with increasing strain (a,b) for 10, (c,d) for 50, and (e,f) for 100.

Figure 8a,c show two HADDF-STEM images of the sample for location F with a strain of 100, and the results of EDS line scanning along the arrows in Figure 8a,c are displayed in Figure 8b,d. Obviously, the EDS line scanning of the precipitate at the grain boundary showed the enrichment of the Cu element. However, the results of EDS analysis along the GB shows that there is little difference in the distribution of elements within grains and at grain boundaries. Figure 8c shows a TEM image of the sample for HPT deformation to strain 100 after heat treatment at 200 °C for 1 h. A high-resolution transmission electron microscope (HRTEM) image of a precipitation located at a grain boundary labeled by a white arrow in Figure 8e is illustrated in Figure 8f. Based on the analysis of the fast Fourier transformation (FFT) pattern of the region marked by a white box in Figure 8f, the precipitate was identified as the Al_2CuMg phase (JCPDS#00-028-014, space group: Cmc m , lattice parameters: $a = 0.4$, $b = 0.925$, $C = 0.715$ nm). The Al_2CuMg particle shown in Figure 8f was

oriented with $[1\bar{3}4]$ zone axis to the electron beam. In addition, microstructural analysis of these precipitations has pointed out that most precipitates located at the intragranular and GBs are Al_2CuMg phase. Only when the torsional deformation reaches a very large strain can a small amount of the Al_2Cu phase precipitate at GBs, which have been reported in the same alloy system in the previous study [32].

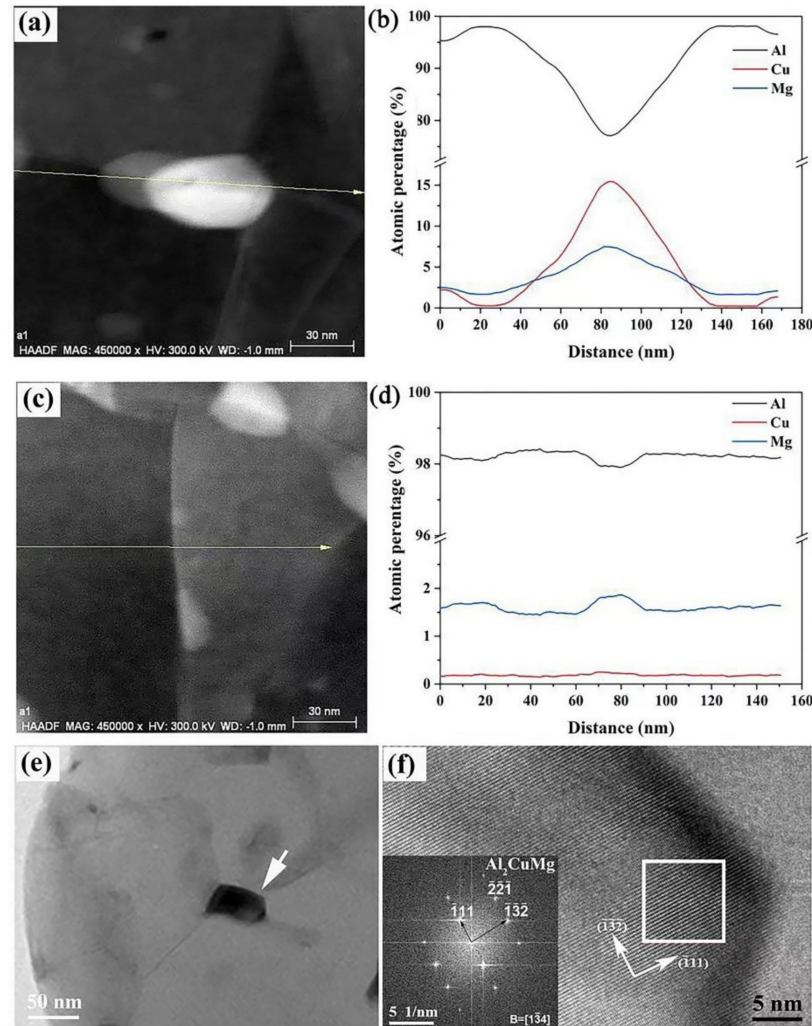


Figure 8. Magnified HADDF-STEM images of (a) precipitated phase located at GB and (c) GB near the GB precipitates; (b,d) corresponding to EDS line scanning profiles of the Al, Cu, and Mg elements along the yellow arrow in (a,c), respectively; (e) TEM micrographs of Al-4Mg-0.3Cu alloy with stain 100 after heat treatment; (f) HRTEM image of the precipitate in Figure 8e and FFT image suggest that the precipitate is Al_2CuMg phase.

Figure 9a demonstrates an EBSD image of a 5-turn sample for location E with strain 50 after heat treatment at 200 °C for 1 h, where grain colors stand for different orientations of the grains, as shown by the inverse pole figure in Figure 9a. The orange and black lines demonstrate the locations of high-angle grain boundaries (HAGBs, with misorientation greater than 15°) and low-angle grain boundaries (LAGBs, with misorientation between 2° and 15°), respectively. The EBSD phase map (Figure 9b) clearly shows that the Al_2CuMg phase mainly distributes along the GBs. The statistics histograms of misorientation angle distribution obtained from Figure 9a are shown in Figure 9c. From Figure 9c, it can be seen that the volume fraction of LAGBs in the as-heated sample for strain 50 is about 9%. There was no precipitated phase distribution at the LAGBs from the heat-treated sample, as marked by black arrows in Figure 9a. In addition, it is seen from Figure 9a that the number

of precipitate distributions at LAGBs is far less than that from the HAGBs. From the above results, it can be inferred that LAGBs suppressed the precipitation of the Al_2CuMg phase, as compared with random HAGBs. Thus, it can be concluded that the nucleation and growth of precipitates at grain boundaries are closely related to the orientation angles between grains: the greater the orientation difference between grains, the more favorable the nucleation and growth of precipitates at grain boundaries. Li et al. also observed that low-energy boundaries lead to a lower density of precipitates in Al-Mg alloy [33].

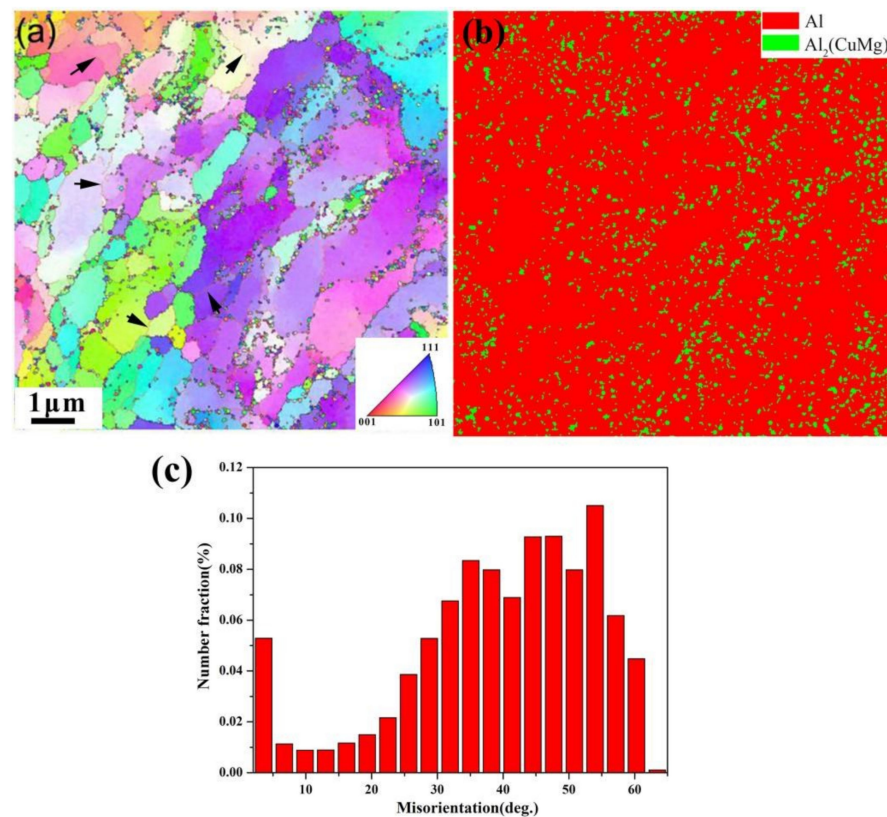


Figure 9. (a) EBSD IPF maps of HPT-processed Al-4Mg-0.3Cu alloy for 5 turns under strain 50 after heating at 200 °C for 1 h; (b) EBSD phase maps for Al matrix and Al_2CuMg precipitations; (c) histograms of the misorientation angles from EBSD IPF maps (a).

During HPT at room temperature, significant modification of the GB structure of an Al-4Mg-0.3Cu sample occurred, as illustrated in Figure 10. Figure 10a–d are bright field images of the edge region of the high-pressure twisted Al-4Mg-0.3Cu alloy for 1, 3, 5, and 10 turns, respectively. Comparing Figure 10a–d, it can be found that the grain boundaries of the submicron grains are gradually flattened; that is, the grain boundaries gradually change from a nonequilibrium state to an equilibrium state. Figure 10a1–d1 are HRTEM images of a region near the grain boundary of the black grain lying in the direction $[110]_{\text{Al}}$ from Figure 10a–d, respectively. Inverse Fourier transformation images A and B of the region marked by a white box in Figure 10a1 show that a lot of dislocations, labeled by “T”, exist in the region near GBs on different $\{111\}$ planes. Similarly, C and D, E and F, and G and H are the inverse fast Fourier transform (IFFT) diagrams along different $\{111\}$ slip planes from Figure 10b1–d1, respectively. It can be found from its IFFT diagrams that the number of dislocations along $\{111\}$ slip planes near the GBs decreases with increasing strain. According to the dislocation density calculation formula, $\rho = n/d^2$, where n is the total number of dislocations along the slip planes and d is the side length of the white box region for the Fourier transform [34]. Therefore, the average dislocation density of the four regions can be calculated as: $2 \times 10^{17} \text{ m}^{-2}$, $4.2 \times 10^{16} \text{ m}^{-2}$, $1.2 \times 10^{16} \text{ m}^{-2}$, $1.0 \times 10^{16} \text{ m}^{-2}$. The evolution trend of dislocation density near the GBs from the submicron-

sized Al-4Mg-0.3Cu alloy can be obtained by TEM measurements; that is, when the grain size is refined to submicron scale, the average dislocation density in the region near GBs decreases. The stacking faults are also observed from Figure 10a1,b1, which may form by partial dislocation emission from GBs. In addition, these high-angle grain boundaries (HAGBs) formed during SPD processing gradually transformed from a nonequilibrium state to an equilibrium state. This result may be connected with the enhanced grain boundary diffusion in a nonequilibrium grain boundary structure, which may also be revealed in nickel-base superalloy [35].

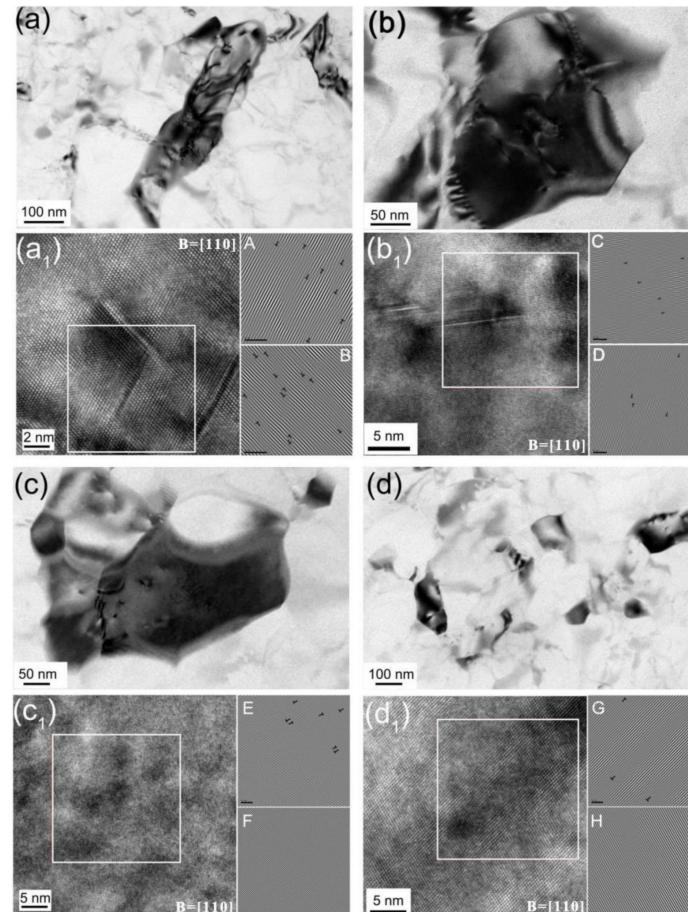


Figure 10. (a–d) demonstrate TEM bright field images from the edge region of an HPT Al-Mg alloy sample for 1, 3, 5, and 10 turns; (a1–d1) show HRTEM images of grains in TEM bright field images (a–d) along the (110) direction; A and B, C and D, E and F, and G and H are the one-dimensional IFFT of images (a1–d1) along the slip plane ($\bar{1}11$) and ($1\bar{1}1$).

The thermal stability of the ultrafine grain Al-4Mg-0.3Cu alloy with a different grain structure was studied through heat treatment at 200 °C for 1 h. The evolution of the average grain size of the samples from locations E and F with strain ~50 and 100 and postannealing is plotted in Figure 11. As illustrated in Figure 11, the average grain size decreases from 140 to 100 nm with a strain increase from 50 to 100. After annealing treatment, the average grain size increases to 800 and 300 nm with strains of 50 and 100.

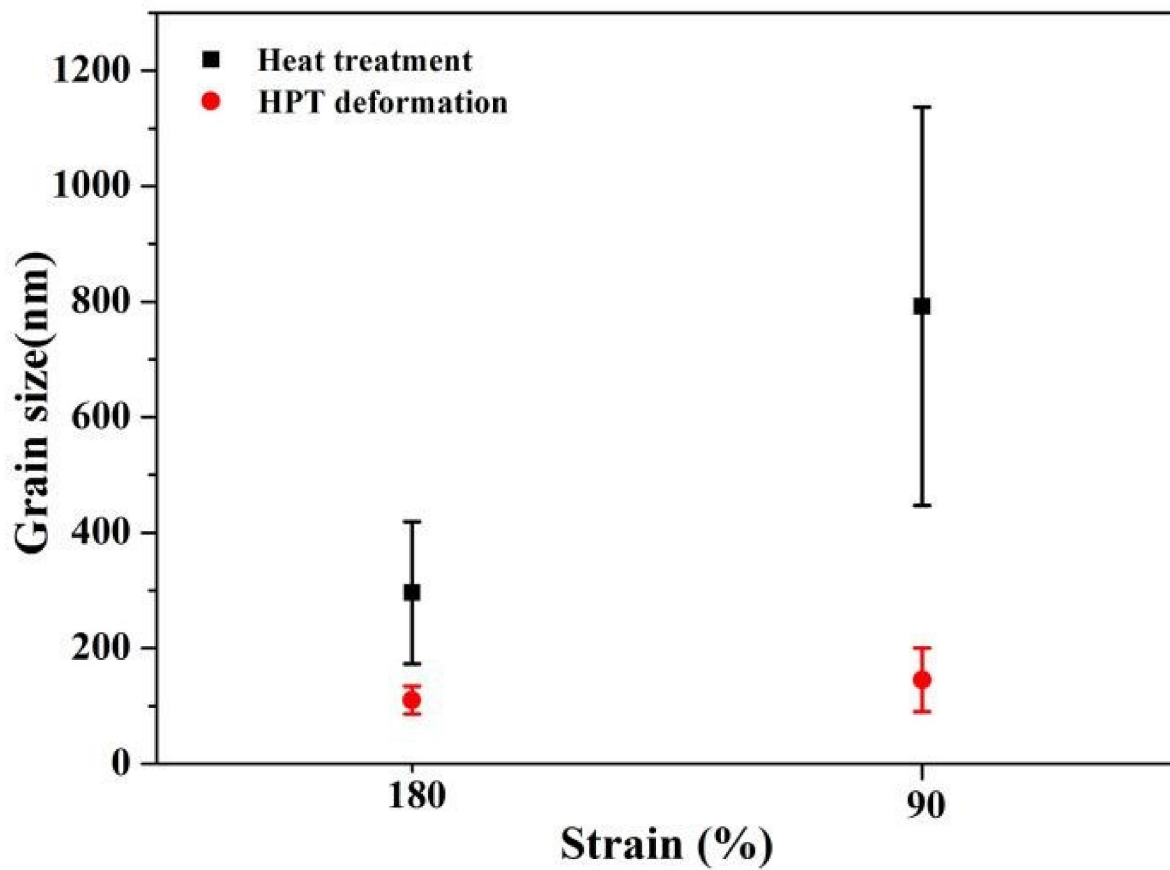


Figure 11. Grain size evolution of the HPT processed Al-4Mg-0.3Cu alloy with strains 50 and 100 and postannealing.

Figure 12a displays the tensile stress–strain curves of as-cast, 5-turn, and 10-turn HPT samples, and the average values of fracture strength and elongation to failure with the scattering range are plotted in Figure 12b. The stress–strain curves shown in Figure 12a,c, have no straight regions prior to plastic deformation, which was attributed that the extensometer was not loaded during the tensile test of the small size samples. Inspection showed that the initial unprocessed sample consistently exhibited the highest elongation to failure and the lowest flow stress. As shown in Figure 12a, the tensile strength significantly increases from 280 MPa for the as-cast state to 750 MPa and 850 MPa for the 5-turn and 10-turn HPT samples. Figure 12c shows the stress–strain curves of the 5-turn and 10-turn HPT samples after heat treatment at 200 °C for 1 h, and the corresponding characteristic parameters with the scattering range are illustrated in Figure 12d. After annealing treatment, the fracture strength of the 5-turn and 10-turn HPT samples has a slight decrease with an increase in fracture elongation, especially for the 5-turn HPT sample.

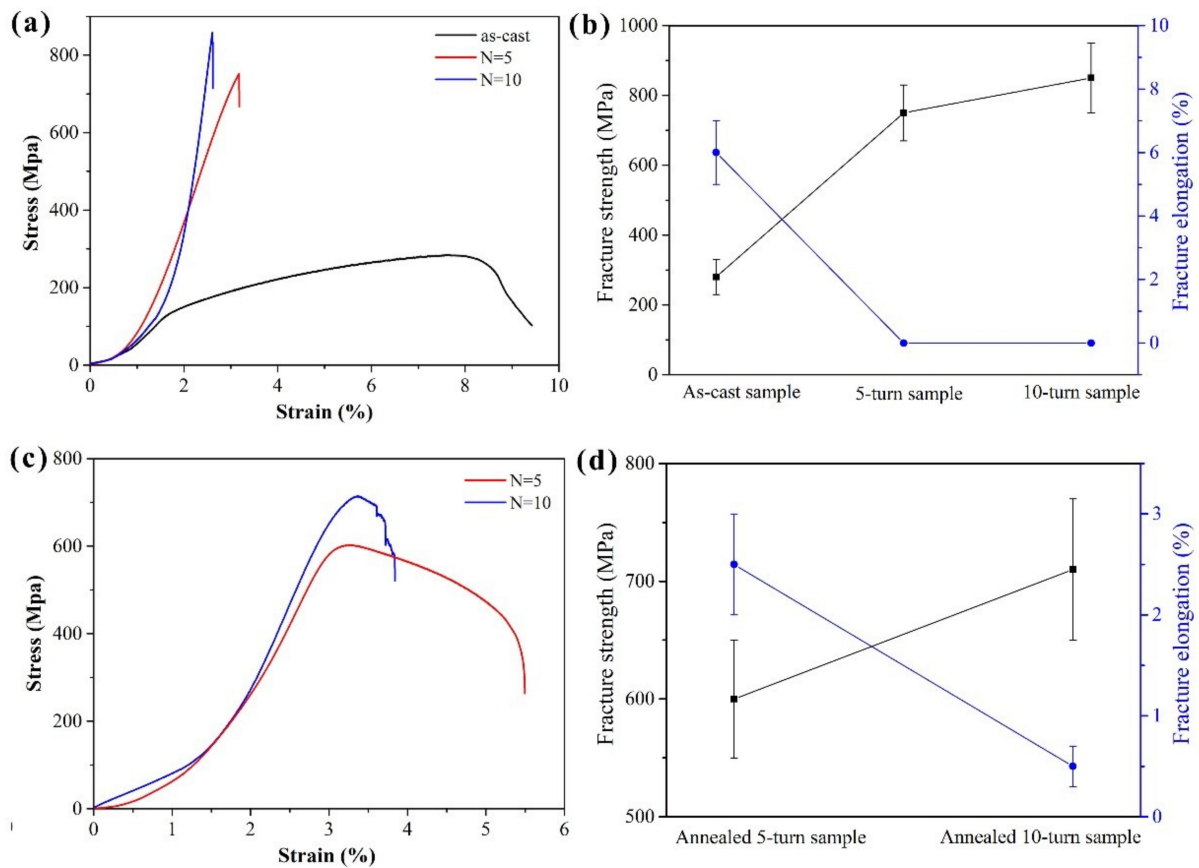


Figure 12. Stress–strain curves of (a) as-cast, 5-turn, and 10-turn HPT samples; (b) statistical summary of fracture strength and fracture elongation for as-cast, 5-turn, and 10-turn HPT samples; (c) stress–strain curves of post-HPT 5-turn and 10-turn samples; (d) statistical summary of fracture strength and fracture elongation for post-HPT 5-turn and 10-turn samples.

4. Discussion

4.1. Impacts of Accumulated Shear Strain on Microstructural Features

As expected, the microstructural characterization of samples is strongly affected by different levels of deformation. Microstructural transformations occur in several steps, which are schematically displayed in Figure 4. In the low plastic strain stage, the plastic-deformation-aroused dislocations first interacted and rearranged to form a lamella grain structure in Figure 4a. At such early stages of deformation, there is a large fraction of low-angle grain boundaries (LAGB). Then, with the increasing deformation, the lamella grain structure is subdivided to dislocation cells with a size of approximately 1.4 μm , and the dislocation cells gradually transform to high-angle grain boundaries, as illustrated in Figure 4c. In the following step, these grains are further refined to the submicron scale, and Shockley partial dislocations can be triggered from the GBs of the ultrafine grains along the slip plane {111} to accommodate plastic deformation. Accompanied by the formation of stacking faults aroused by partial dislocation emission from GBs, the GBs of the ultrafine grains gradually transform from nonequilibrium state into equilibrium state. Finally, a steady state is reached that an equiaxed ultrafine grain structure with high-angle grain boundaries and random orientation has an average grain size 100 nm. It is now well accepted that coarse-grain refinement in the HPT process is dominated by the well-known dislocation subdivision mechanism.

4.2. Mechanism of Cu Segregation and Its Influence on Thermal Stability

Experimental results and computational simulations have pointed out that the ultrafine-structured Al alloys processed by SPD can trigger the solute segregation along GBs to

minimize the Gibbs free energy [36,37]. Until now, the mechanism of SPD-induced solute segregation in Al alloys is summarized as follows: the solute drag mechanism by moving boundaries and the solute–vacancy annihilation mechanism at GBs [38]. In this experiment, solute segregation along the GBs was found only when the Al-4Mg-0.3Cu alloy was refined to the ultrafine scale, as shown in Figure 8. Obviously, the solute drag mechanism cannot give a reasonable explanation of the above phenomenon. In addition, the segregation of Cu at GBs was observed in this work, which is clearly different from that frequently reported in the previous literature [39]. Therefore, understanding the role of minor Cu addition to Al-4Mg alloy on solute diffusion is a key factor to reveal the Cu segregation.

It has been generally recognized that the diffusion of substitutional solute was mainly vacancy-mediated [40]. Therefore, strain-induced vacancy among all crystalline defects created during SPD is a key factor in influencing the atomic mobility and promoting GB segregation [41]. Solute atoms may combine with vacancies to form solute–vacancy and solute–solute–vacancy complexes [42]. In Al-Mg-Cu alloys, the formation energy of vacancy–solute complexes continuously decreases as the number of solute atoms increases. The stability of vacancy–solute complexes mainly arises from the Mg-Cu bonds formed with the increasing number of solute atoms [43]. Interaction between solute–vacancy complexes can assist in the formation of solute clusters which were dragged by dislocations [44]. S. Medrano et al. [21] revealed that trace Cu addition to Al-Mg alloy can initiate the formation of Mg-Cu–vacancy clusters with a high content of Mg and clean Cu in the Al-3Mg alloy with 0.2 wt.% Cu. Apart from this, several studies indicated the presence of nanoscale Mg-Cu coclusters in the matrix of Al-Cu-Mg alloy processed by HPT using the atom probe tomography technology [42,45]. Therefore, the high Mg–low Cu atomic complexes dragged by dislocations can exist in the matrix, which lead to a lower diffusivity of solute Mg compared with that of Al-Mg alloy without Cu. On the other hand, energetic binding between vacancies and solute atoms can also affect the diffusion behavior. One example of the latter behavior can be seen in the observed decreased response of Al-Cu to natural aging with microalloying additions of Sn, which is attributed to a strong Sn–vacancy starving the formation of Cu–vacancy [46]. The energetic binding of Cu–vacancy (0.02 eV) is more positive compared with that of Mg–vacancy (−0.02 eV) in Al alloy, where positive binding energies indicate an energetically favorable binding [41]. Therefore, a strong Cu–vacancy binding energy could suppress the formation of Mg–vacancy pairs, thereby slowing down the Mg diffusion towards GBs. The flux of Cu–vacancy annihilated towards GBs can induce a pronounced segregation of Cu at GBs. In addition, the SPD can induce GB segregations but does not lead to intensive precipitation, which is also confirmed in the ternary Al–Cu–Mg alloy processed by HPT [47]. Meanwhile, the GBs with Cu segregation usually have high orientation mismatch between two adjacent grains, and difficulties were observed at GBs with low-angle grain boundaries.

GB segregations driven by minimization of the grain boundary energy suppressed the boundary mobility, and eventually reduced the driving force for grain growth [39]. In addition to GB segregation, dislocation–solute atom interactions can also drag the GB and enhance the thermal stability [48]. The slow growth of grain size in the sample with a strain of 100 may be attributed to the GB precipitation formation, as illustrated in Figure 9. In fact, the thermal stability of Al alloys can be enhanced if GBs are pinned by particles (so-called Zener pinning) or segregations, which could also help stabilize UFG structures by reducing the driving force for grain growth.

4.3. Effects of Solute Segregation/Precipitation on Mechanical Properties

The hardness values from Vickers microhardness measurements demonstrated a strain hardening behavior with increasing torsional straining, and a high level of homogeneous microstructure was achieved when the torsional strain was beyond 80. Previous research results pointed out that minor Cu addition in Al-Mg alloy processed by HPT only caused a slight increase in hardness due to solute–defect interaction [49]. XRD analysis and TEM observation showed that as the density of dislocations in the grain increases beyond a cer-

tain critical value, dislocations will start to cluster to form cell walls, which will ultimately develop into full grain boundaries; and further dislocations can also be subsumed into existing grain boundaries. Thus, on further straining beyond the stage where the critical dislocation density is reached, increasing grain boundary strengthening dominates the further increase in hardness. In addition, strain-induced grain boundary segregations can lead to a significant extra mechanical strength, as reported for Al-Cu alloy [50]. Therefore, the significant increase in hardness from 50 Hv for the center position to 220 Hv for the edge position from the 10-turn HPT disk sample is mainly attributed to the grain refinement and Cu GB segregation.

The fracture mode rapidly transforms from ductile fracture for an as-cast sample to brittle fracture for 5-turn and 10-turn HPT samples. Based on the microstructural analysis, the strength increase in the HPT processing sample is mainly due to dislocation strengthening, grain refinement, and GB strengthening. In the literature, when the grain size of Al-4Mg alloy is refined to ultrafine scale (with grain size lesser than 1 μm), the deformation of the alloy is mainly associated with the “dislocations-grain boundary” mechanism [34]. This specific feature is attributed to an increase in the critical stress necessary to nucleate dislocations from boundaries covered by solutes [17], which can explain the increased fracture strength of 10-turn HPT samples compared with that of 5-turn HPT samples. In addition, Cu segregation at GBs of Al alloys can induce the creation of new Cu-Al bonds and enhance the fracture strength [51]. Therefore, the cooperative interaction of the high densities of GBs and Cu segregation has resulted in the observed significantly higher strength of the Al-4Mg-0.3Cu alloy with strain beyond ~ 100 . Meanwhile, the fracture elongation decrease in the 5-turn and 10-turn HPT samples is attributed to the fact that the lattice dislocation increment from Frank–Read sources was suppressed at the ultrafine grain scale.

Microscopy analysis of the 10-turn HPT samples subjected to heat treatment revealed that the average grain size has a slight increase and dense Al_2CuMg precipitations mainly located at GBs. The stress–strain curves exhibited an average fracture strength of 720 MPa and a slightly increasing fracture elongation. A higher uniform elongation of $\sim 2.5\%$ was achieved for the 5-turn HPT samples after annealing treatment due to a grain size growth of approximately to 1 μm , which arose from the enhancement of dislocation-coordinated plastic deformation. Meanwhile, a high density of precipitates in a 5-turn HPT sample after heat treatment enhanced the solute–dislocations interactions, which partially compensated for a reduction in strength due to grain size growth. Therefore, these results suggest that the Al-4Mg-0.3Cu alloy processed by HPT annealing in an optimal condition can attain an excellent combination of fracture strength and fracture elongation.

5. Conclusions

This study presents the influence of a minor Cu addition to Al-4Mg alloy subjected to HPT deformation and subsequent annealing treatment on the microstructural evolution, thermal stability, and mechanical properties. The following findings and conclusions are obtained.

1. The grain refinement process and GB evolution feature were clarified with increasing strain through TEM. HADDF-STEM and EDS line scanning revealed that a high proportion of Cu-segregated GBs were prone to generation with a lower degree of nonequilibrium.
2. The mechanism for solute Cu segregation at GBs was clarified from the view of the binding energy of solute–vacancy. In addition, the EBSD image from the post-aging sample showed that the Al_2CuMg phase was prone to precipitating at the HAGBs compared with the LAGBs.
3. The thermal stabilities of different grain structures were evaluated through aging treatment at 200 $^\circ\text{C}$ for 1 h. A microstructural analysis by TEM suggested that the segregation of Cu can induce a dense distribution of the Al_2CuMg phase, which plays an important role in the enhancement of thermal stability.

4. Tensile strengths of ~750 and 850 MPa were achieved in the Al-4Mg-0.3Cu alloy by HPT processing for 5 and 10 turns. The subsequent aging after HPT processing significantly increased the tensile fracture elongation, especially for a 5-turn sample, despite that the fracture strength was slightly decreasing.

Author Contributions: X.Y.: conceptualization, writing—original draft preparation, supervision; C.G.: investigation, resources, formal analysis; T.K.: conceptualization, methodology, writing—review and editing; W.Y.: investigation, data curation, formal analysis; Y.G.: conceptualization, methodology, writing—review and editing; L.W.: resources, investigation, visualization; H.C.: conceptualization, methodology, visualization; X.L.: conceptualization, methodology, writing—review and editing; R.H.: resources, visualization, data curation; J.C.: resources, visualization, data curation. All authors have read and agreed to the published version of the manuscript.

Funding: This research was supported by the Natural Science Foundation of Shanxi Province (No. 20210302124195); the Scientific and Technological Innovation Programs of Higher Education Institutions in Shanxi, China (No. 2019L0650); Taiyuan University of Science and Technology Scientific Research Initial Funding (Nos. 20192063 and 20102029); and Innovation Project of postgraduate education in Shanxi Province (No. 2021Y677).

Data Availability Statement: All data, models, and codes generated or used during the study appear in the submitted article.

Conflicts of Interest: No conflict of interest exists in the submission of this manuscript, and the manuscript is approved by all authors for publication. I would like to declare on behalf of my coauthors that the work described was original research that has not been published previously. All the authors listed have approved the manuscript that is enclosed.

References

1. Santos, M.C.; Machado, A.R.; Sales, W.F.; Barrozo, M.A.S.; Ezugwu, E.O. Machining of aluminum alloys: A review. *Int. J. Adv. Manuf. Technol.* **2016**, *86*, 3067–3080. [[CrossRef](#)]
2. Hirsch, J. Recent development in aluminium for automotive applications. *Trans. Nonferrous Met. Soc. China* **2014**, *24*, 1995–2002. [[CrossRef](#)]
3. Hirsch, J. Aluminium in Innovative Light-Weight Car Design. *Mater. Trans.* **2011**, *52*, 818–824. [[CrossRef](#)]
4. Wang, H.; Geng, H.; Zhou, D.; Niitsu, K.; Muránsky, O.; Zhang, D. Multiple strengthening mechanisms in high strength ultrafine-grained Al–Mg alloys. *Mater. Sci. Eng. A* **2019**, *771*, 138613. [[CrossRef](#)]
5. Cho, C.-H.; Son, H.-W.; Lee, J.-C.; Son, K.-T.; Lee, J.-W.; Hyun, S.-K. Effects of high Mg content and processing parameters on Portevin-Le Chatelier and negative strain rate sensitivity effects in Al–Mg alloys. *Mater. Sci. Eng. A* **2020**, *779*, 139151. [[CrossRef](#)]
6. Zha, M.; Li, Y.; Mathiesen, R.H.; Børge, R.; Roven, H.J. Achieve high ductility and strength in an Al–Mg alloy by severe plastic deformation combined with inter-pass annealing. *Mater. Sci. Eng. A* **2014**, *598*, 141–146. [[CrossRef](#)]
7. Zhilyaev, A.P.; Langdon, T.G. Using high-pressure torsion for metal processing: Fundamentals and applications. *Prog. Mater. Sci.* **2008**, *53*, 893–979. [[CrossRef](#)]
8. Meng, C.; Hu, W.; Sandlöbes, S.; Korte-Kerzel, S.; Gottstein, G. The effect of large plastic deformation on elevated temperature mechanical behavior of dynamic strain aging Al–Mg alloys. *Acta Mater.* **2019**, *181*, 67–77. [[CrossRef](#)]
9. Mei, X.; Mei, Q.; Li, J.; Li, C.; Wan, L.; Chen, F.; Chen, Z.; Xu, T.; Wang, Y.; Tan, Y. Solid-state alloying of Al–Mg alloys by accumulative roll-bonding: Microstructure and properties. *J. Mater. Sci. Technol.* **2022**, *125*, 238–251. [[CrossRef](#)]
10. Zhou, D.; Bu, Y.; Muránsky, O.; Geng, H.; Sun, B.; Yang, C.; Zhang, D. Annealing-induced strengthening and stabilization in ultrafine-grained Al and Al–Mg alloys prepared by rapid powder consolidation. *Mater. Sci. Eng. A* **2022**, *833*, 142539. [[CrossRef](#)]
11. Xu, W.; Zhang, B.; Du, K.; Li, X.; Lu, K. Thermally stable nanostructured Al–Mg alloy with relaxed grain boundaries. *Acta Mater.* **2022**, *226*, 117640. [[CrossRef](#)]
12. Zha, M.; Zhang, H.-M.; Meng, X.-T.; Jia, H.-L.; Jin, S.-B.; Sha, G.; Wang, H.-Y.; Li, Y.-J.; Roven, H.J. Stabilizing a severely deformed Al–7Mg alloy with a multimodal grain structure via Mg solute segregation. *J. Mater. Sci. Technol.* **2021**, *89*, 141–149. [[CrossRef](#)]
13. Sauvage, X.; Enikeev, N.; Valiev, R.; Nasedkina, Y.; Murashkin, M. Atomic-scale analysis of the segregation and precipitation mechanisms in a severely deformed Al–Mg alloy. *Acta Mater.* **2014**, *72*, 125–136. [[CrossRef](#)]
14. Devaraj, A.; Wang, W.; Vemuri, V.R.; Kovarik, L.; Jiang, X.; Bowden, M.; Trelewicz, J.; Mathaudhu, S.; Rohatgi, A. Grain boundary segregation and intermetallic precipitation in coarsening resistant nanocrystalline aluminum alloys. *Acta Mater.* **2019**, *165*, 698–708. [[CrossRef](#)]
15. Duchaussoy, A.; Sauvage, X.; Edalati, K.; Horita, Z.; Renou, G.; Deschamps, A.; De Geuser, F. Structure and mechanical behavior of ultrafine-grained aluminum-iron alloy stabilized by nanoscaled intermetallic particles. *Acta Mater.* **2019**, *167*, 89–102. [[CrossRef](#)]
16. Sauvage, X.; Cuvilly, F.; Russell, A.; Edalati, K. Understanding the role of Ca segregation on thermal stability, electrical resistivity and mechanical strength of nanostructured aluminum. *Mater. Sci. Eng. A* **2020**, *798*, 140108. [[CrossRef](#)]

17. Mohammadi, A.; Enikeev, N.A.; Murashkin, M.Y.; Arita, M.; Edalati, K. Developing age-hardenable Al-Zr alloy by ultra-severe plastic deformation: Significance of supersaturation, segregation and precipitation on hardening and electrical conductivity. *Acta Mater.* **2021**, *203*, 116503. [[CrossRef](#)]
18. Chinh, N.Q.; Valiev, R.Z.; Sauvage, X.; Varga, G. Grain boundary segregation and unique plastic behaviour in an ultrafinegrained Al-Zn alloy processed by HPT. *Adv. Eng. Mater.* **2014**, *16*, 1000–1009. [[CrossRef](#)]
19. Straumal, B.; Valiev, R.; Kogtenkova, O.; Zieba, P.; Czepe, T.; Bielanska, E.; Faryna, M. Thermal evolution and grain boundary phase transformations in severely deformed nanograined Al-Zn alloys. *Acta Mater.* **2008**, *56*, 6123–6131. [[CrossRef](#)]
20. Yuan, L.; Peng, L.; Han, J.; Liu, B.; Wu, Y.; Chen, J. Effect of Cu addition on microstructures and tensile properties of high-pressure die-casting Al-5.5Mg-0.7Mn alloy. *J. Mater. Sci. Technol.* **2019**, *35*, 1017–1026. [[CrossRef](#)]
21. Medrano, S.; Zhao, H.; Gault, B.; De Geuser, F.; Sinclair, C. A model to unravel the beneficial contributions of trace Cu in wrought Al-Mg alloys. *Acta Mater.* **2021**, *208*, 116734. [[CrossRef](#)]
22. Shuai, L.; Huang, T.; Yu, T.; Wu, G.; Hansen, N.; Huang, X. Segregation and precipitation stabilizing an ultrafine lamellar-structured Al-0.3%Cu alloy. *Acta Mater.* **2021**, *206*, 116595. [[CrossRef](#)]
23. Nasedkina, Y.; Sauvage, X.; Bobruk, E.; Murashkin, M.Y.; Valiev, R.; Enikeev, N. Mechanisms of precipitation induced by large strains in the Al-Cu system. *J. Alloys Compd.* **2017**, *710*, 736–747. [[CrossRef](#)]
24. Edalati, K.; Horita, Z.; Langdon, T.G. The significance of slippage in processing by high-pressure torsion. *Scr. Mater.* **2009**, *60*, 9–12. [[CrossRef](#)]
25. Edalati, K.; Hashiguchi, Y.; Pereira, P.H.R.; Horita, Z.; Langdon, T.G. Effect of temperature rise on microstructural evolution during high-pressure torsion. *Mater. Sci. Eng. A* **2018**, *714*, 167–171. [[CrossRef](#)]
26. Lutterotti, L.; Gialanella, S. X-ray diffraction characterization of heavily deformed metallic specimens. *Acta Mater.* **1998**, *46*, 101–110. [[CrossRef](#)]
27. Williamson, G.K.; Smallman, R.E., III. Dislocation densities in some annealed and cold-worked metals from measurements on the X-ray debye-scherrer spectrum. *Philos. Mag.* **1956**, *1*, 34–46. [[CrossRef](#)]
28. Azushima, A.; Kopp, R.; Korhonen, A.; Yang, D.Y.; Micari, F.; Lahoti, G.D.; Groche, P.; Yanagimoto, J.; Tsuji, N.; Rosochowski, A.; et al. Severe plastic deformation (SPD) processes for metals. *CIRP Ann.* **2008**, *57*, 716–735. [[CrossRef](#)]
29. Estrin, Y.; Molotnikov, A.; Davies, C.H.J.; Lapovok, R. Strain gradient plasticity modelling of high-pressure torsion. *J. Mech. Phys. Solids* **2008**, *56*, 1186–1202. [[CrossRef](#)]
30. Smallman, R.E.; Westmacott, K.H. Stacking faults in face-centred cubic metals and alloys. *Philos. Mag. A J. Theor. Exp. Appl. Phys.* **1957**, *2*, 669–683. [[CrossRef](#)]
31. Chen, Y.; Gao, N.; Sha, G.; Ringer, S.P.; Starink, M.J. Microstructural evolution, strengthening and thermal stability of an ultrafine-grained Al-Cu-Mg alloy. *Acta Mater.* **2016**, *109*, 202–212. [[CrossRef](#)]
32. Yang, X.; Li, K.; An, X.; Ni, S.; Wei, W.; Du, Y.; Song, M. Influence of deformation microstructure on the precipitation behaviors of an Al-4Mg-0.3Cu alloy. *J. Alloys Compd.* **2017**, *695*, 2238–2245. [[CrossRef](#)]
33. Xu, W.; Xin, Y.; Zhang, B.; Li, X. Stress corrosion cracking resistant nanostructured Al-Mg alloy with low angle grain boundaries. *Acta Mater.* **2022**, *225*, 117607. [[CrossRef](#)]
34. Yang, X.; Ni, S.; Song, M. Partial dislocation emission in a superfine grained Al-Mg alloy subject to multi-axial compression. *Mater. Sci. Eng. A* **2015**, *641*, 189–193. [[CrossRef](#)]
35. Razumovskii, I.; Kornelyuk, L.; Valiev, R.; Sergeev, V. Diffusion along nonequilibrium grain boundaries in a nickel-base superalloy. *Mater. Sci. Eng. A* **1993**, *167*, 123–127. [[CrossRef](#)]
36. Lei, T.; Shin, J.; Gianola, D.S.; Rupert, T.J. Bulk nanocrystalline Al alloys with hierarchical reinforcement structures via grain boundary segregation and complex ion formation. *Acta Mater.* **2021**, *221*, 117394. [[CrossRef](#)]
37. Edalati, K.; Bachmaier, A.; Beloshenko, V.A.; Beygelzimer, Y.; Blank, V.D.; Botta, W.J.; Bryła, K.; Čížek, J.; Divinski, S.; Enikeev, N.A.; et al. Nanomaterials by severe plastic deformation: Review of historical developments and recent advances. *Mater. Res. Lett.* **2022**, *10*, 163–256. [[CrossRef](#)]
38. Sauvage, X.; Duchaussoy, A.; Zaher, G. Strain Induced Segregations in Severely Deformed Materials. *Mater. Trans.* **2019**, *60*, 1151–1158. [[CrossRef](#)]
39. Koju, R.; Mishin, Y. Atomistic study of grain-boundary segregation and grain-boundary diffusion in Al-Mg alloys. *Acta Mater.* **2020**, *201*, 596–603. [[CrossRef](#)]
40. Seyedrezai, H.; Grebennikov, D.; Mascher, P.; Zurob, H.S. Study of the early stages of clustering in Al-Mg-Si alloys using the electrical resistivity measurements. *Mater. Sci. Eng. A* **2009**, *525*, 186–191. [[CrossRef](#)]
41. Wolverson, C. Solute-vacancy binding in aluminum. *Acta Mater.* **2007**, *55*, 5867–5872. [[CrossRef](#)]
42. Nagai, Y.; Murayama, M.; Tang, Z.; Nonaka, T.; Hono, K.; Hasegawa, M. Role of vacancy-solute complex in the initial rapid age hardening in an Al-Cu-Mg alloy. *Acta Mater.* **2001**, *49*, 913–920. [[CrossRef](#)]
43. Peng, J.; Bahl, S.; Shyam, A.; Haynes, J.A.; Shin, D. Solute-vacancy clustering in aluminum. *Acta Mater.* **2020**, *196*, 747–758. [[CrossRef](#)]
44. Wu, S.; Soreide, H.S.; Bin Chen, B.; Bian, J.; Yang, C.; Li, C.; Zhang, P.; Cheng, P.; Zhang, J.; Peng, Y.; et al. Freezing solute atoms in nanograined aluminum alloys via high-density vacancies. *Nat. Commun.* **2022**, *13*, 1–11. [[CrossRef](#)]
45. Liu, M.; Liu, Z.; Bai, S.; Xia, P.; Ying, P.; Wang, A. Analysis on the dissolution behavior of various size Cu-Mg co-clusters near a fatigue crack tip of underaged Al-Cu-Mg alloy during cyclic loading. *J. Alloys Compd.* **2017**, *699*, 119–125. [[CrossRef](#)]

46. Lotter, F.; Petschke, D.; De Geuser, F.; Elsayed, M.; SEXTL, G.; Staab, T.E.M. In situ natural ageing of Al-Cu-(Mg) alloys: The effect of In and Sn on the very early stages of decomposition. *Scr. Mater.* **2019**, *168*, 104–107. [[CrossRef](#)]
47. Chen, Y.; Gao, N.; Sha, G.; Ringer, S.P.; Starink, M.J. Strengthening of an Al-Cu-Mg alloy processed by high-pressure torsion due to clusters, defects and defect-cluster complexes. *Mater. Sci. Eng. A* **2015**, *627*, 10–20. [[CrossRef](#)]
48. Koju, R.; Mishin, Y. Direct atomistic modeling of solute drag by moving grain boundaries. *Acta Mater.* **2020**, *198*, 111–120. [[CrossRef](#)]
49. Zhang, J.; Gao, N.; Starink, M.J. Al–Mg–Cu based alloys and pure Al processed by high pressure torsion: The influence of alloying additions on strengthening. *Mater. Sci. Eng. A* **2010**, *527*, 3472–3479. [[CrossRef](#)]
50. Jia, H.; Bjørge, R.; Cao, L.; Song, H.; Marthinsen, K.; Li, Y. Quantifying the grain boundary segregation strengthening induced by post-ECAP aging in an Al-5Cu alloy. *Acta Mater.* **2018**, *155*, 199–213. [[CrossRef](#)]
51. Zhao, D.; Løvvik, O.M.; Marthinsen, K.; Li, Y. Segregation of Mg, Cu and their effects on the strength of Al Σ 5 (210)[001] symmetrical tilt grain boundary. *Acta Mater.* **2018**, *145*, 235–246. [[CrossRef](#)]

Disclaimer/Publisher’s Note: The statements, opinions and data contained in all publications are solely those of the individual author(s) and contributor(s) and not of MDPI and/or the editor(s). MDPI and/or the editor(s) disclaim responsibility for any injury to people or property resulting from any ideas, methods, instructions or products referred to in the content.